Integrated control of braking energy regeneration and pneumatic anti-lock braking

J-Z Zhang*, **X Chen,** and **P-J Zhang**
State Key Laboratory of Automotive Safety and Energy, Tsinghua University, Beijing, People's Republic of China

The manuscript was received on 6 July 2009 and was accepted after revision for publication on 24 November 2009.

DOI: 10.1243/09544070JAUTO1307

Abstract: This paper mainly focuses on integrated control of the brake system of a hybrid electric vehicle, i.e. the integration of friction braking and regenerative braking during anti-lock braking control and series brake blending during normal deceleration. Based on a series regenerative braking system, the structure of an integrated brake system is proposed. The models of each part of a hybrid electric bus are built in MATLAB–Simulink, taking authorized articles as references. A test bench with the original pneumatic brake system of a bus is also built to carry out hardware-in-the-loop (HIL) tests of the integrated brake system and to study the characteristics of the system better. The integrated control strategy is proposed on the basis of a pneumatic anti-lock braking strategy. Simulation results show that the participation of regenerative braking in the anti-lock braking control can be beneficial to both the ride comfort and the braking performance of the vehicle. HIL test results validate the results of the simulations. An integrated brake controller is designed and made to carry out the control strategies on board. A field in which further research could be carried out is also proposed.

Keywords: regenerative braking, anti-lock braking system, simulation, hardware-in-the-loop tests, brake controller, hybrid electric city bus

1 INTRODUCTION

The ever-heavier burden on the environment and energy requires automobiles to be cleaner and more efficient. Among the solutions proposed for motor vehicles, electric vehicles, including fuel cell hybrid electric vehicles (HEVs), internal combustion HEVs, and plug-in electric vehicles, are the most promising.

Studies show that, in urban driving, about one third to one half of the energy of the power plant is consumed during braking [**1**, **2**]. Among the key features of electric vehicles, regenerative braking can improve the fuel economy effectively by recovering the braking energy. As the most developed and commercialized electric vehicle, the HEV with an internal combustion engine (ICE) usually has regenerative braking as the threshold of its concept. A vehicle featuring idle-off but no regenerative braking is commonly not considered to be an HEV [**3**]. The effect of regenerative braking may vary depending on the HEV configuration. It is claimed that vehicle fuel economy can be enhanced by up to 15 per cent through the application of regenerative braking [**4**].

Regenerative braking control strategies can be divided into series or parallel types. The parallel strategy is relatively simple, exerting the braking torque of the electric motor via transmission on the wheels without modulating the frictional braking torque apart from the control of the driver. In the series strategy a regenerative braking torque is exerted and the frictional braking torque modulated, targeting the need to give a certain overall braking torque according to the stroke of the braking pedal. Thus, the series strategy for regenerative braking is also called the strategy of 'brake blending' [**5**]. It is obvious that, under the series strategy, more braking energy can be recaptured. It also indicates that the frictional braking system inherited from an ordinary ICE automobile should be amended to allow blending of the frictional braking force and the regenerative braking force. However, the flexibility and the

**Corresponding author: State Key Laboratory of Automotive Safety and Energy, Tsinghua University, Beijing 100084, People's Republic of China.*
email: jzhzhang@tsinghua.edu.cn

better capacity of the regenerating braking energy are really attractive. Increasingly, HEV manufacturers have begun to adopt the series regenerative braking strategy. Taking Honda for example, the 2006 Civic hybrid was the first Honda to feature blending of frictional and regenerative braking [**6**].

Meanwhile an anti-lock braking system (ABS) has long been made a compulsory device on board by legislators around the world. As an example, in 1996, the National Highway Traffic Safety Administration amended the Federal Motor Vehicle Safety Standard 121 [**7**] to require an ABS on all new heavy vehicles [**8**].

Series regenerative braking and anti-lock braking share a common feature, namely modulation of the frictional brake force. As most of the present HEVs have been developed in the past decade, anti-lock braking will be present. Thus, the coordination of regenerative braking and anti-lock braking and even the integration of the two types of braking are of great interest to automobile manufacturers and institutes. Kusano [**9**] proposed a brake pressure control device aimed at the integration of regenerative braking and anti-lock braking that is believed to be installed in the Prius. Continental Teves are a main supplier of brakes and active safety devices in Europe and have developed an integrated brake system for regenerative braking and anti-lock braking for the Escape hybrid sport utility vehicle of Ford [**10**]. Honda, as mentioned above, developed an integrated brake master cylinder to carry out this function, which is relatively sophisticated in structure [**11**]. TRW's solution is based on a traditional booster-master cylinder, and its modulation of the braking force is carried out by adjusting the boosting force of the booster [**5**]. Chu *et al.* [**12**] proposed a solution for the coordination of regenerative braking and anti-lock braking based on a pneumatic brake system for buses and coaches; however, the strategy for regenerative braking is parallel. Progress in developing an integrated brake system based on a pneumatic brake is yet to be revealed.

The present authors have carried out the research and development of regenerative braking for a couple of years. A series regenerative braking system has been developed and tested on two hybrid buses, namely a hydrogen–natural gas (HCNG) hybrid city bus sponsored by the US Department of Energy and a fuel cell hybrid city bus as a project under the Chinese 'National 863 Key Project' [**13**]. In order to further the research and to ensure the braking safety and efficiency of a vehicle under both normal deceleration and emergency brakes, integrated control of regenerative braking and anti-lock braking based on a pneumatic brake system has been studied. The topology is based on the already developed brake system with series regenerative braking. The anti-lock braking control strategy takes some open documents as reference and has been proved to function well. In order to facilitate the research, a set of models, including those of the tyre, the vehicle, and the pneumatic system, has been built. A pneumatic brake system test bench with pneumatic modulating valves is also built to simulate a system on board better. The integrated system for regenerative braking and anti-lock braking and its strategy have been simulated and hardware-in-the-loop (HIL) tested. An experimental integrated brake controller is designed and made to carry out the control strategies on board. Some results are presented in this article.

2 SYSTEM LAYOUT

2.1 Pneumatic brake system with series regenerative braking

In previous research, a regenerative braking system has been developed and applied on vehicles which are rear-wheel-drive serial hybrid buses with pneumatic frictional brakes. Figure 1 shows the diagram of the whole system.

Two modulating valves distinguish the system from an ordinary frictional service brake system for a bus. These valves modulate the pneumatic brake force under the control of the vehicle controller to cooperate with the regenerative brake force of the electric motor and are of the same type as those adopted in a pneumatic ABS. A separate ABS from WABCO is installed for braking under extreme conditions.

The control strategy is a typical series type, taking into consideration the electric bus voltage, the battery state of charge (SOC), and the velocity of the vehicle. The system can recapture more than 50 per cent of the braking energy that formerly would be dissipated by frictional brakes under some circumstances [**13**]. It contributes a reduced fuel consumption of 15 per cent on the fuel cell hybrid bus under the Chinese City Bus Driving Cycle. The test results on fuel economy are presented in Table 1. A better performance can be expected after further optimization.

2.2 Integrated brake system with regenerative braking and anti-lock braking

As can be seen from the layout of the regenerative braking system above, there are two sets of pneu-

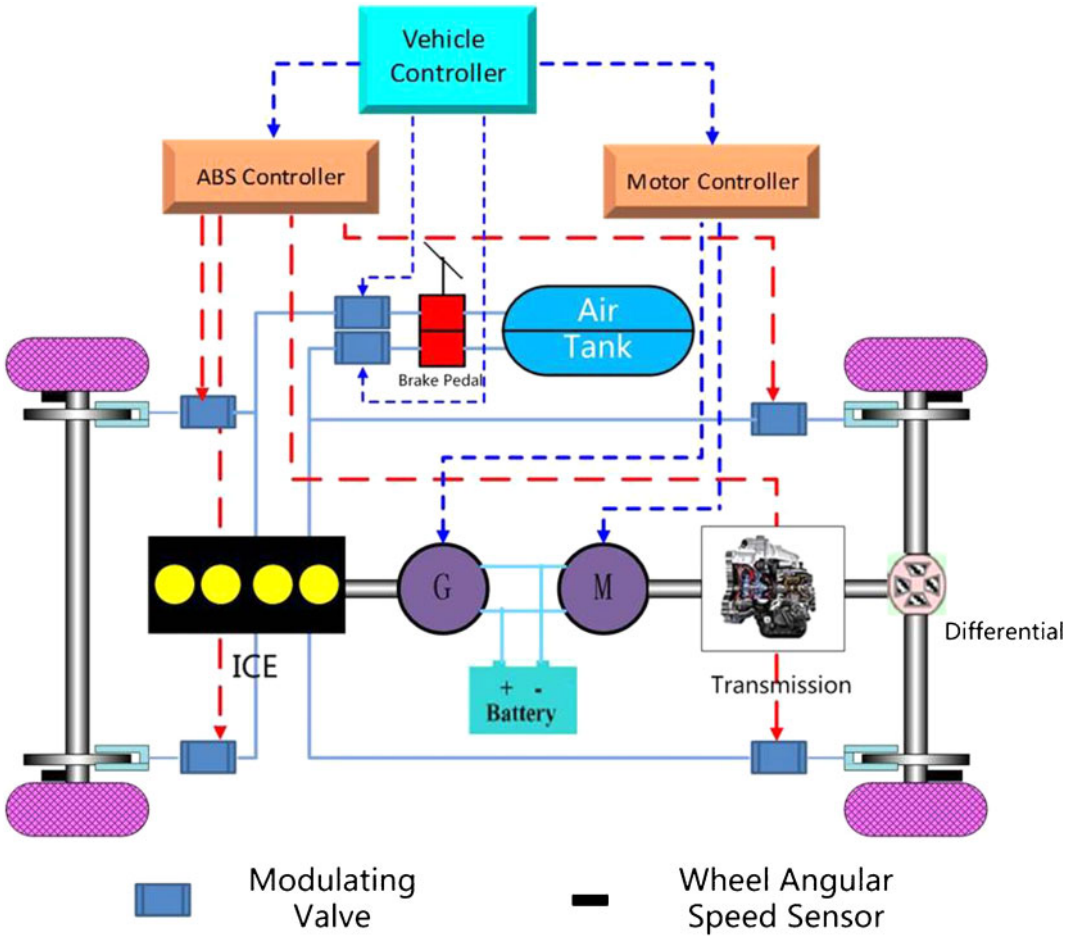

Fig. 1 Diagram of the series regenerative braking system

Table 1 Effect of the series regenerative braking system

	H_2 consumption by fuel cell stacks (kg/100 km)	Equivalent H_2 consumption of battery output (kg/100 km)	Equivalent H_2 consumption overall (kg/100 km)
Series regenerative braking	7.18	0.34	7.52
Non-regenerative braking	8.19	0.66	8.85
Fuel consumption reduced by regenerative braking		15.03%	

matic modulating valves. One set of valves is responsible for air pressure modulation during normal deceleration (brake blending); the other set of valves belongs to the separate ABS as modulators during anti-lock braking control.

There are mainly two disadvantages of the previous system involving regenerative braking and anti-lock braking. First, as the two sets of valves are under the control of the vehicle control unit and anti-lock braking control unit respectively, some of the modulators are redundant. It is possible to use the same set of valves to carry out the same functions. Second, there is a barrier between the two control units, thus making it difficult to modulate the regenerative braking when anti-lock braking control is required. As a source of brake force, the motor torque of regenerative braking can be helpful in anti-lock braking control; this will be discussed later in this article.

Figure 2 illustrates the diagram of the proposed integrated brake system with regenerative braking and anti-lock braking. A brake controller takes over the control of all the four modulating valves. It also communicates with the motor controller via the vehicle controller to give a regenerative torque command and to receive a motor torque limit. During normal decelerations, the brake controller modulates the pneumatic pressure by controlling the modulating valves while requiring a regenerative torque. Thus, brake blending can be carried out.

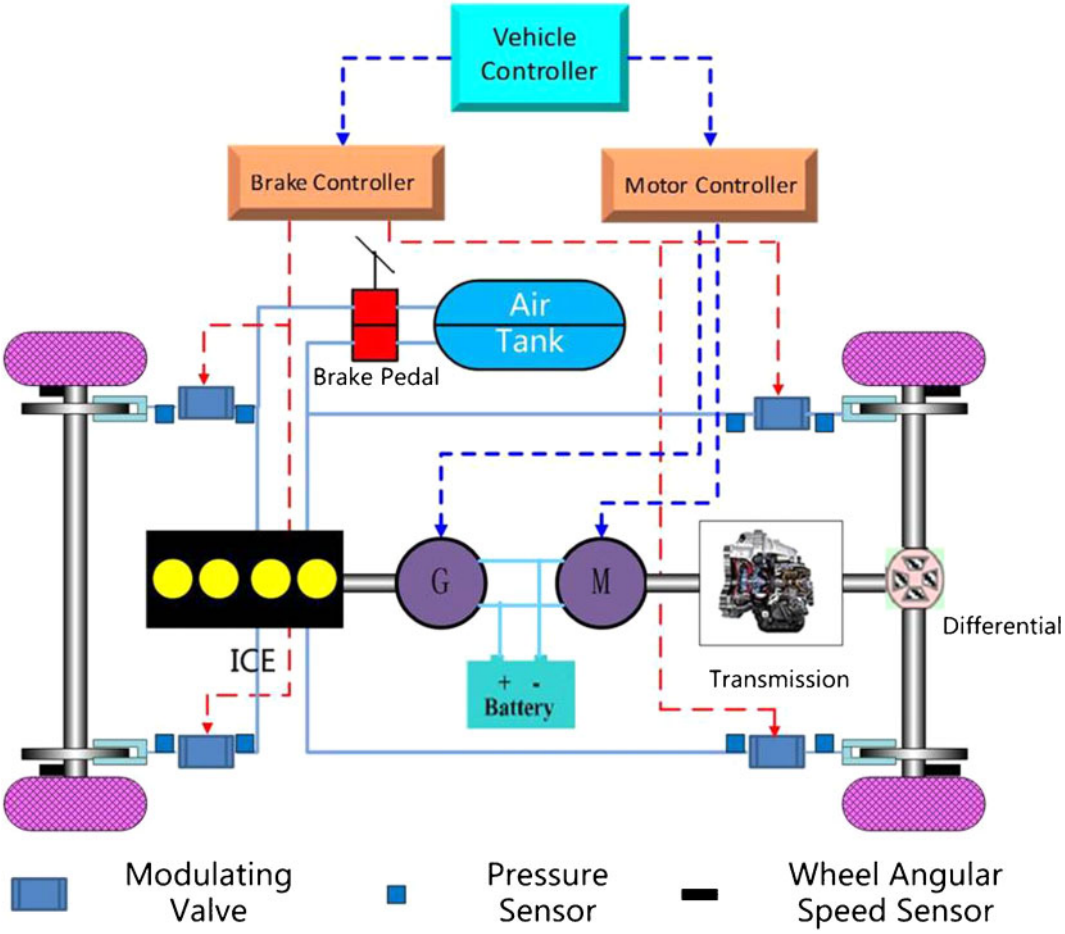

Fig. 2 Diagram of the integrated brake system

Wheel speed sensors monitoring the speeds of the four wheels are connected to the brake controller as well. When there is a need for anti-lock braking control by the control strategy, the brake control unit modulates the pneumatic pressure as an ABS controller but meanwhile gives out a motor torque command. The frictional brake and the regenerative brake cooperate with each other to avoid wheel locking and to maintain the stability of the vehicle, although fuel economy is not the first priority under those circumstances.

3 MODELLING THE SYSTEM

Simulation is a crucial step of research and development nowadays. Simulation results provide useful information for optimizing the structure and the control strategy of the system on condition that the model is rational. In order to carry out the simulation method of research, appropriate models of every part of the vehicle including the brake system will be built. This involves the vehicle (overall dynamics), the battery, the tyres, the electric motor, and the pneumatic system.

3.1 Vehicle dynamics

The research at present mainly focuses on the longitudinal motion of the vehicle during braking, but it is obvious that the lateral motion and steering are crucial in the research relative to anti-lock braking control. Thus, a model of vehicle dynamics with 15 degrees of freedom has been built.

An $O_1X_1Y_1Z_1$ coordinate system will be defined first, which is static relative to the space. The origin O_1 coincides with the centre of gravity of the vehicle at the beginning of braking, while the axis O_1X_1 is in the longitudinal direction of the vehicle, pointing forwards. The plane $O_1X_1Y_1$ is parallel to the ground and the axis O_1Z_1 is perpendicular to the ground, pointing upwards. The $OXYZ$ coordinate system, which is fixed with respect to the vehicle, has its origin at the centre of gravity of the vehicle. OX is in the longitudinal direction of the vehicle, pointing forwards. The plane

OXY is parallel to the ground with OZ perpendicular to OXY, pointing upwards. Both coordinate systems are right handed. The yaw angle of the vehicle, the roll angle of the sprung mass, and the pitch angle of the sprung mass are denoted by Y_{aw}, φ, and θ respectively, and their vectors are in the OZ, OX, and OY directions respectively.

The 15 degrees of freedom of the vehicle model are as follows: the displacements of the vehicle along O_1X_1 and O_1Y_1, which are denoted by x and y respectively; the vertical motion of the sprung mass of the vehicle along OZ, which is denoted by z; the yaw angle ϕ, the roll angle φ, and the pitch angle θ; the vertical motions of the four wheels, which are denoted by z_{FL}, z_{FR}, z_{RL}, and z_{RR}; the rotations of the four wheels, as represented by the rotational speeds ω_{FL}, ω_{FR}, ω_{RL}, and ω_{RR}; the steering angle δ of the front wheels.

The displacements along O_1X_1 and O_1Y_1 can also be expressed in terms of u, the velocity along OX, and v, the velocity along OY, in the OXY coordinate system, according to

$$\begin{aligned}\dot{x} &= u\cos\phi - v\sin\phi \\ \dot{y} &= u\sin\phi + v\cos\phi\end{aligned} \tag{1}$$

The equations of the motions are as follows (Fig. 3). The longitudinal motion of the vehicle is given by

$$\begin{aligned}&m\left(\dot{u}-\ddot{\phi}v\right)+m_s\left(2e_0\dot{\varphi}\dot{\phi}+e_0\varphi\ddot{\phi}+D_0\ddot{\theta}\right) \\ &\quad=(F_{xFL}+F_{xFR})\cos\delta-(F_{yFL}+F_{yFR})\sin\delta+F_{xRL} \\ &\qquad+F_{xRR}\end{aligned} \tag{2}$$

the transverse motion of the vehicle by

$$\begin{aligned}&m\left(\dot{v}+\dot{\phi}u\right)+m_s\left(2D_0\dot{\theta}\dot{\phi}+D_0\theta\ddot{\phi}-e_0\ddot{\varphi}\right) \\ &\quad=(F_{xFL}+F_{xFR})\sin\delta-(F_{yFL}+F_{yFR})\cos\delta+F_{yRL} \\ &\qquad+F_{yRR}\end{aligned} \tag{3}$$

the vertical motion of the sprung mass by

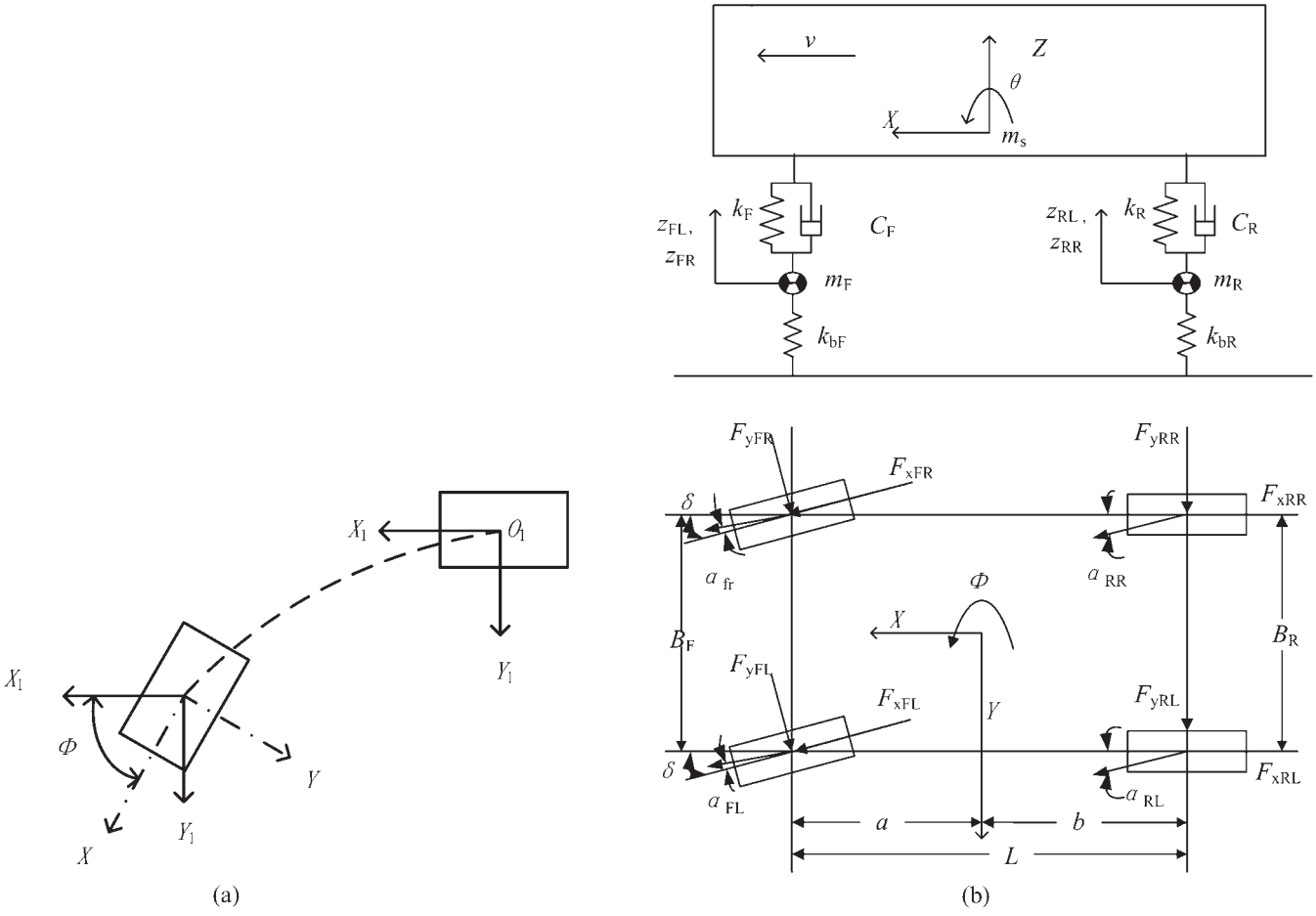

Fig. 3 Diagram of (a) the coordinate systems and (b) the vehicle model

$$m_s\ddot{z} = -F_{sFL} - F_{sFR} - F_{sRL} - F_{sRR} \tag{4}$$

the yaw of the vehicle by

$$\begin{aligned} &J_z\ddot{\phi} + m_s(\dot{u}e_0\varphi + \dot{v}D_0\theta + uD_0\theta\dot{\phi} - ve_0\varphi\dot{\phi}) \\ &= \frac{B_F}{2}\left[(-F_{xFL} + F_{xFR})\cos\delta - (-F_{yFL} + F_{yFR})\sin\delta\right] \\ &\quad + \frac{B_R}{2}(-F_{xRL} + F_{xRR}) \\ &\quad + a\left[(F_{xFL} + F_{xFR})\sin\delta + (F_{yFL} + F_{yFR})\cos\delta\right] \\ &\quad - b(F_{yRL} + F_{yRR}) \end{aligned} \tag{5}$$

the pitching motionof the sprung mass by

$$\begin{aligned} &J_y\ddot{\theta} + m_s\dot{u}D_0 + m_se_0D_0\varphi\ddot{\phi} + 2m_se_0D_0\dot{\varphi}\dot{\phi} - m_svD_0\dot{\phi} \\ &= aF_{sFL} + aF_{sFR} - bF_{sRL} - bF_{sRR} \end{aligned} \tag{6}$$

the rolling motion of the sprung mass by

$$\begin{aligned} &J_x\ddot{\varphi} - m_s\dot{v}e_0 - m_se_0D_0\theta\ddot{\phi} - 2m_se_0D_0\dot{\theta}\dot{\phi} - m_sue_0\dot{\phi} \\ &= \frac{1}{2}B_F(F_{sFR} - F_{sFL}) + \frac{1}{2}B_R(F_{sRR} - F_{sRL}) \end{aligned} \tag{7}$$

the vertical motions of the wheels by

$$\begin{aligned} m_{Fw}\ddot{z}_{FL} &= F_{sFL} - k_{bF}z_{FL} \\ m_{Fw}\ddot{z}_{FR} &= F_{sFR} - k_{bF}z_{FR} \\ m_{Rw}\ddot{z}_{RL} &= F_{sRL} - k_{bR}z_{RL} \\ m_{Rw}\ddot{z}_{RR} &= F_{sRR} - k_{bR}z_{RR} \end{aligned} \tag{8}$$

and the forces of the suspension that have been mentioned above by

$$\begin{aligned} F_{sFL} &= k_F\left(z - z_{FL} - a\theta + \frac{1}{2}B_{FF}\varphi\right) \\ &\quad + C_F\left(\dot{z} - \dot{z}_{FL} - a\dot{\theta} + \frac{1}{2}B_{FF}\dot{\varphi}\right) \\ F_{sFR} &= k_F\left(z - z_{FR} - a\theta - \frac{1}{2}B_{FF}\varphi\right) \\ &\quad + C_F\left(\dot{z} - \dot{z}_{FR} - a\dot{\theta} - \frac{1}{2}B_{FF}\dot{\varphi}\right) \\ F_{sRL} &= k_R\left(z - z_{RL} + b\theta + \frac{1}{2}B_{RR}\varphi\right) \\ &\quad + C_R\left(\dot{z} - \dot{z}_{RL} + b\dot{\theta} + \frac{1}{2}B_{RR}\dot{\varphi}\right) \\ F_{sRR} &= k_R\left(z - z_{RR} + b\theta - \frac{1}{2}B_{RR}\varphi\right) \\ &\quad + C_R\left(\dot{z} - \dot{z}_{RR} + b\dot{\theta} - \frac{1}{2}B_{RR}\dot{\varphi}\right) \end{aligned} \tag{9}$$

Note that ϕ, θ, φ, $\dot{\phi}$, $\dot{\theta}$, $\dot{\varphi}$, $\ddot{\phi}$, $\ddot{\theta}$, and $\ddot{\varphi}$ are taken as first-order small quantities. In the equations above, the small quantities which are of third order or above were eliminated. In the equation for the yaw of the vehicle, the self-aligning torques of the four wheels are also eliminated. m is the overall mass of the vehicle. m_s is the sprung mass of the vehicle. z_{xx} denotes the vertical motion of the wheel xx, where xx = FL for the front left wheel, FR for the front right wheel, RL for the rear left wheel, and RR for the rear right wheel. m_{xxw} denotes the mass of the wheel xx, where xx is as defined above. F_{xxx} is the tangential force of the wheel xx, F_{yxx} is the transverse force of the wheel xx, and F_{sxx} is the force of the suspension on the wheel xx, where xx is as defined above. J_x, J_y, and J_z are the moments of inertia of the vehicle in the OX, OY, and OZ directions respectively. A is the longitudinal distance from the centre of gravity of the vehicle to the front axle. b is the longitudinal distance from the centre of gravity of the vehicle to the rear axle. l is the wheelbase. Thus, $l = a + b$. B_F and B_R are the widths of the front track and the rear track respectively. B_{FF} and B_{RR} are the distances between the two joints of suspension for the front axle and the rear axle respectively. D_0 is the vertical distance between the centre of gravity for the sprung mass and the pitching axle, which coincides with OY. e_0 is the vertical distance between the centre of gravity for the sprung mass and the rolling axle, which coincides with OY. k_{bF} and k_{bR} are the stiffnesses for a single front wheel and a single rear wheel respectively. k_F and k_R are the stiffnesses for a single spring of the front suspension and a single spring of the rear suspension respectively. C_F and C_R are the damping coefficients of a single damper of the front suspension and a single damper of the rear suspension respectively.

3.2 The tyre

The tyre model is very important for research on braking, and especially on anti-lock braking. The model should be able to simulate the real tyre in both adhesion and sliding.

The tyre model proposed by Gim and Nikravesh [**14**] is analytical. It is capable of simulating the tyre under a pure slip ratio, a pure slip angle, a pure camber angle, and a combination of all three. Gim and Nikravesh stated that the longitudinal stress may be assumed to depend on the longitudinal stiffness and the longitudinal elastic deformation in the adhesion region and to depend on the contact pressure and the tyre–road friction coefficient in the sliding region.

Research on regenerative braking and anti-lock braking focuses mainly on longitudinal motions at present. Only pure slip is considered.

The motion of the tyre of an idle wheel can be expressed as

$$J_{\mathrm{w}}\dot{\omega} = F_x R - T_{\mathrm{b}} \tag{10}$$

The motion of the tyre of a drive wheel can be expressed as

$$\left(J_{\mathrm{w}} + \frac{1}{2}J_{\mathrm{pt}}\right)\dot{\omega} = F_x R - T_{\mathrm{b}} + T_{\mathrm{d}} \tag{11}$$

J_{w} is the moment of inertia of the wheel, and J_{pt} is the moment of inertia of the powertrain which is shared between the two drive wheels. Ω is the rotational speed of the wheel; thus, $\dot{\omega}$ is the rotational acceleration of the wheel. F_x is the longitudinal force exerted on the wheel by the ground. T_{b} is the friction brake torque applied on the wheel, and T_{d} is the driving torque applied on the wheel. Note that T_{d} can be negative, indicating a regenerative braking force.

The longitudinal force exerted on the wheel by the ground depends on the slip ratio and the characteristics of the tyre. The slip ratio of tyre during braking is defined as

$$S_{\mathrm{S}} = \frac{V - \omega r}{V} \tag{12}$$

where S_{S} is the longitudinal slip ratio, V is the velocity of the vehicle, ω is the rotational speed of the wheel, and r is the nominal radius of the tyre. Note that the denominator is taken as the velocity of the vehicle in braking.

The friction coefficient μ, which in longitudinal driving or braking is equal to the longitudinal friction coefficient μ_x, can be expressed as

$$\mu = \mu_0\left(1 - A_{\mathrm{s}}^* S_{\mathrm{S}}\right) \tag{13}$$

where μ_0 is the friction parameter at zero sliding velocity, A_{s}^* is the friction reduction factor, and S_{S} is the absolute value of the slip ratio. A_{s}^* can be determined by μ_0 and μ_1. μ_1 can be the friction parameter at any other sliding velocity and usually is the value at $S_{\mathrm{S}} = 1$. Thus, the friction coefficient decreases linearly as S_{S} increases.

Between the adhesion region and the sliding region there is a breakaway point. l_{n} is defined as the non-dimensional contact patch length of the adhesion region, and S_{n} is defined as the non-dimensional contact patch length of the sliding region. This yields the equation

$$S_{\mathrm{n}} = 1 - l_{\mathrm{n}} \tag{14}$$

The position of the breakaway point, or the value of S_{n}, is determined by the longitudinal friction coefficient μ_x, the normal force F_z between the tyre and the road surface, and the longitudinal stiffness C_{S} according to

$$S_{\mathrm{n}} = \frac{C_{\mathrm{S}} S_{\mathrm{S}}}{3\mu_x F_z} \tag{15}$$

As $0 \leqslant S_{\mathrm{n}} \leqslant 1$, a critical (maximum) slip ratio which allows a longitudinal elastic deformation can be stated as

$$S_{\mathrm{SC}} = \frac{3\mu_x F_z}{C_{\mathrm{S}}} \tag{16}$$

The longitudinal force between the tyre and the road surface can be expressed as

$$F_\xi = \begin{cases} 3\mu_x F_z S_{\mathrm{n}}\left(1 - S_{\mathrm{n}} + \frac{1}{3}S_{\mathrm{n}}^2\right) & \text{for } S_{\mathrm{S}} \leqslant S_{\mathrm{SC}} \\ \mu_x F_z & \text{for } S_{\mathrm{S}} > S_{\mathrm{SC}} \end{cases} \tag{17}$$

It can be seen from the equations above that the friction coefficient μ at every S_{S} and the longitudinal stiffness C_{S} are critical for the determination of the longitudinal force. Gim and Nikravesh [**15**] presented several sets of experimental data, including the slip ratio–longitudinal force curves. However, the data were obtained from experiments on tyres of a passenger car, giving different loads on the tyres and different geometrical parameters of the tyres. The data indicated that the longitudinal stiffness is proportional to the normal force on the tyres. Meanwhile, the relation between the longitudinal stiffness and the geometric parameters of the tyres was suggested by Bohm [**16**]. Thus, by data extrapolation and geometry calculation, the longitudinal stiffness of the front tyre can be reasonably chosen as 342 545 N/slip, and that of the rear tyre as 588 954 N/slip.

According to the Gim–Nikravesh tyre model, the characteristics of the longitudinal force of the front wheel on different surfaces are illustrated in Fig. 4. The equivalent friction parameter is defined as the ratio of the longitudinal force to the normal force. Note that the equivalent friction parameter is calculated as if there were no load transfer. In actual braking, the equivalent friction parameter may differ slightly at every slip ratio. The characteristics of the rear wheels are similar to those of the front wheels.

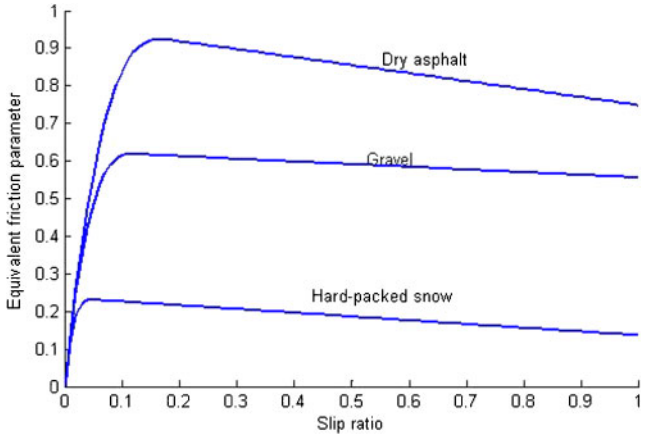

Fig. 4 The equivalent friction parameter of the front wheel

3.3 The battery

The battery model is based on the model of the nickel–metal hydride (NiMH) batteries of a General Motors electric vehicle in ADVISOR. Its original capacity was 60 A h with look-up tables based on previous SOC and temperature data, thereby producing the charging–discharging internal resistance of the battery. The look-up tables are updated with data from the General Research Institute for Nonferrous Metals in the People's Republic of China, which is the manufacturer of the 80 A h NiMH battery utilized in the HCNG vehicle. The model's input is the power required by the electric motor. Its output includes the SOC, the voltage at the output port of battery, the current, and the temperature of the battery.

3.4 The electric motor

The model of the electric motor was built according to the data from the supplier and some test results.

The HCNG hybrid bus and the fuel cell hybrid bus are equipped with electric motors that are products of the Zhuzhou Electric Locomotive Research Institute. The overall efficiency of the motor system including the electric motor and its controller while driving is illustrated as an efficiency map in Fig. 5. The outer characteristic of the electric motor system

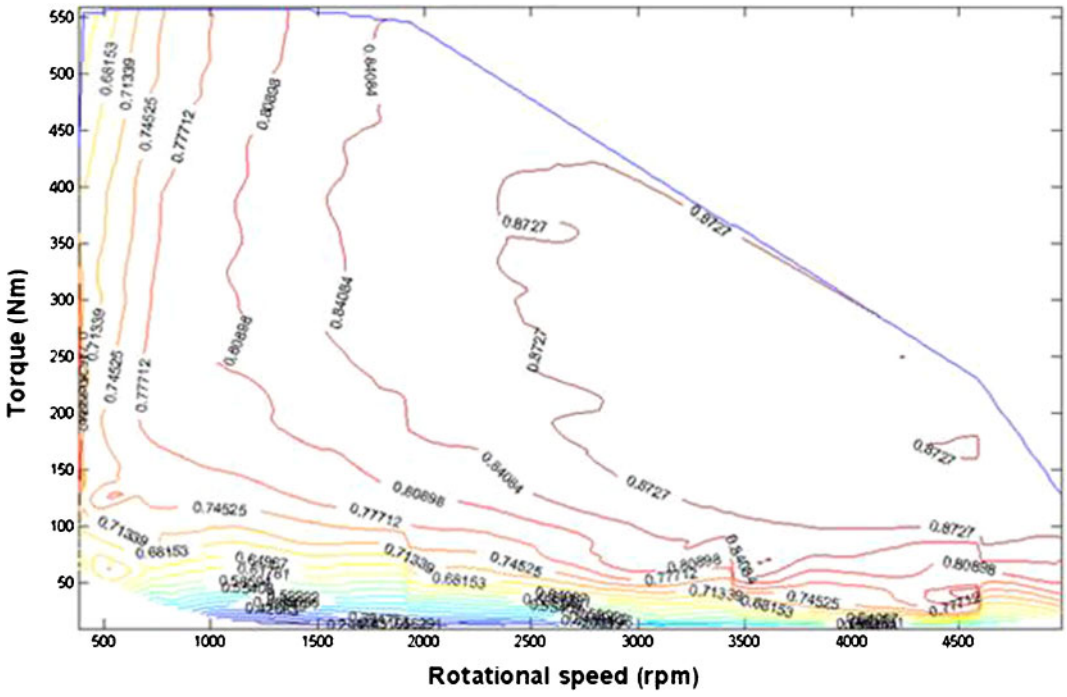

Fig. 5 The efficiency map of the electric motor system

is also shown in the figure. The efficiency map in the regenerative braking mode has almost the same symmetry as that in the driving mode with respect to the axis of rotational speed.

The electric motor and its controller are so tuned that the output torque of the motor covers 95 per cent of the change in the required torque in approximately 0.6 s. Thus, the electric motor system can be expressed as the lag tache and the efficiency map. The transfer function of the first order is

$$G(s) = \frac{1}{0.02s+1} \tag{18}$$

3.5 The pneumatic system

Subramanian *et al.* [**17**] proposed a model for the pneumatic subsystem of an S-cam air brake system, which is the same type of brake with which the HCNG hybrid bus is equipped. The model was built taking into consideration the dynamics of the treadle valve, the dynamics of the brake chamber, and the airflow in the system. Subramanian *et al.* not only built a model of the pneumatic system but also validated it by experiment. The model was able to simulate the system properly. Subramanian *et al.* also provided the parameters of the pneumatic system. The size of the brake chamber, the radius of the pipe, and the working pressure are the same as for the pneumatic brake system with which the HCNG hybrid bus is equipped. Therefore, it is rational to apply the same model when simulating the pneumatic subsystem in the integrated brake system.

When studying the integrated control of regenerative braking and anti-lock braking, the airflow and the motion of the piston propelled by the brake chamber are of most interest. Thus, the airflow part and the brake chamber part are considered to be as in reference [**17**]. Subramanian *et al.* stated that for various test runs the value of the Mach number was found not to exceed 0.2, ensuring that the effects of compressibility of air for the flow through the hose can be neglected. Applying mass balance to the control volume yields

$$\dot{m}_b = \rho u A_p \tag{19}$$

where $\dot{m}_b$ is the time rate of change in the mass of air in the control volume as in Fig. 6, which contains the brake chamber and a part of the hose. P is the density of air inside the control volume at any

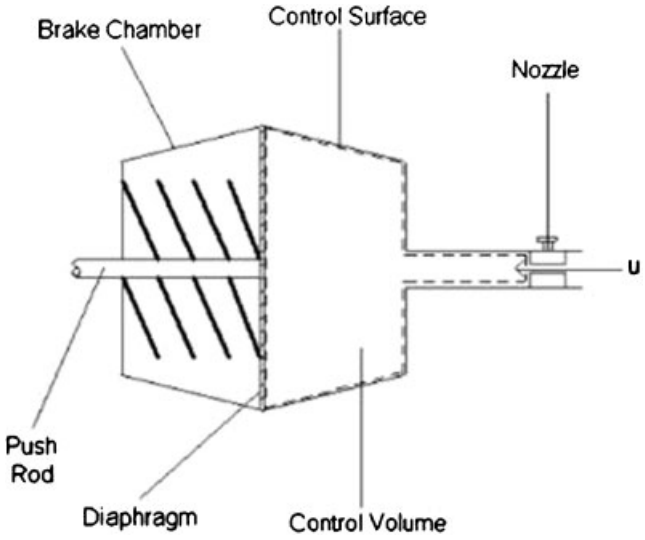

Fig. 6 The brake chamber as the control volume

instant of time. U is the velocity of air at the exit section of the nozzle, which is the velocity of air entering the control volume. A_p is the cross-sectional area of the valve opening.

The velocity of air can be expressed as

$$u = C_D \left\{ \frac{2\gamma}{\gamma-1} \frac{P_0}{\rho_0} \left| \left[1 - \left(\frac{P_b}{P_0} \right)^{(\gamma-1)/\gamma} \right] \right| \right\}^{1/2} \mathrm{sgn}(P_0 - P_b) \tag{20}$$

where C_D is a discharge coefficient compensating for the losses during the flow. Subramian *et al.* [**17**] took C_D equal to 0.82. In the pneumatic subsystem of the integrated brake system, C_D is taken as equal to 0.7, considering the complexity of the system. The signum function above is defined as

$$\mathrm{sgn}(P_0 - P_b) = \frac{P_0 - P_b}{|P_0 - P_b|} \tag{21}$$

Treating the air in the control volume as an ideal gas, a function can be obtained as

$$\dot{m}_b = \frac{1}{\gamma} \frac{\dot{P}_b V_b}{R T_b} + \frac{P_b \dot{V}_b}{R T_b} \tag{22}$$

where P_b is the local pressure inside the control volume, V_b is the volume of the control volume, and T_b is the local temperature inside the control volume at that instant of time. R is the gas constant for air. Γ is the ratio of the specific heats, which is defined as

$$\gamma = \frac{c_P}{c_V} \tag{23}$$

in which c_P is the specific heat of air at constant pressure and c_V is the specific heat of air at constant volume.

The function of the mass of air in the control volume can be specified by the phases of operation of the brake chamber diaphragm. The volume of air inside the control volume at any instant of time can be written as

$$V_b = \begin{cases} V_{01} & \text{if } P_b < P_t \\ V_{01} + A_b x_b & \text{if } 0 < x_b < x_{b\,max} \\ V_{02} & \text{if } x_b = x_{b\,max} \end{cases} \tag{24}$$

in which V_{01} is the initial volume of air in the control volume before the application of the brake, V_{02} is the maximum volume of air in the control volume, A_b is the cross-sectional area of the brake chamber, x_b is the stroke of the brake chamber diaphragm, i.e. the stroke of the push rod, x_{bmax} is the maximum stroke of the push rod, and P_t is the 'push-out' pressure. $P_b < P_t$ corresponds to the phase when $x_b = 0$.

Then, equation (21) can be written as

$$\dot{m}_b = \begin{cases} \dfrac{V_{01}}{\gamma R T_b}\dot{P}_b & \text{if } P_b < P_t \\ \dfrac{V_b}{\gamma R T_b}\dot{P}_b + \dfrac{P_b A_b}{R T_b}\dot{x}_b & \text{if } 0 < x_b < x_{b\,max} \\ \dfrac{V_{02}}{\gamma R T_b}\dot{P}_b & \text{if } x_b = x_{b\,max} \end{cases} \tag{25}$$

Neglecting the inertia of the brake chamber diaphragm, the equation of motion of the brake chamber diaphragm can be written as

$$x_b = \frac{(P_b - P_{atm})A_b - F_{kbi}}{K_b} \tag{26}$$

where F_{kbi} is the preload force of the spring in the brake chamber. Then, equation (24) can be written as

$$\dot{m}_b = \begin{cases} \dfrac{V_{01}}{\gamma R T_b}\dot{P}_b & \text{if } P_b < P_t \\ \left(\dfrac{V_b}{\gamma R T_b} + \dfrac{P_b A_b^2}{R T_b K_b}\right)\dot{P}_b & \text{if } 0 < x_b < x_{b\,max} \\ \dfrac{V_{02}}{\gamma R T_b}\dot{P}_b & \text{if } x_b = x_{b\,max} \end{cases} \tag{27}$$

Comparing equation (26) and equation (18), a governing equation for the pressure transients in the brake chamber during the apply phase can be obtained as

$$\frac{2\gamma}{\gamma - 1}\frac{1}{RT_0}\left|\left[\left(\frac{P_b}{P_0}\right)^{2/\gamma} - \left(\frac{P_b}{P_0}\right)^{(\gamma+1)/\gamma}\right]\right|^{1/2} A_p C_D P_0 \operatorname{sgn}(P_0 - P_b) = \begin{cases} \dfrac{V_{01}P_0^{(\gamma-1)/\gamma}}{\gamma R T_0 P_b^{(\gamma-1)/\gamma}}\dot{P}_b & \text{if } P_b < P_t \\ \left(\dfrac{V_b P_0^{(\gamma-1)/\gamma}}{\gamma R T_b} + \dfrac{P_b^{1/\gamma} A_b^2 P_0^{(\gamma-1)/\gamma}}{R T_b K_b}\right)\dot{P}_b & \text{if } 0 < x_b < x_{b\,max} \\ \dfrac{V_{02}P_0^{(\gamma-1)/\gamma}}{\gamma R T_0 P_b^{(\gamma-1)/\gamma}}\dot{P}_b & \text{if } x_b = x_{b\,max} \end{cases} \tag{28}$$

where P_0 is the supply pressure. Most of the parameters in the pneumatic subsystem model are identical to those in reference [**17**]. However, some of the parameters, including the discharge coefficient C_D, are redefined by experiment on the HIL test bench, which will be introduced later in this article.

The friction brake torque is assumed to be applied on the drum when the push rod is fully pushed out, i.e. when $x_b = x_{bmax}$. The ratio K_{pb} of the pneumatic pressure to the brake torque ratio is acquired during brake testing of the HCNG hybrid bus according to

$$T_b = K_{pb} P_b \tag{29}$$

As mentioned above, T_b is the friction brake torque applied on the wheel and P_b is the pneumatic pressure in the brake chamber.

On the front axle the ratio is 1258.2 N m/bar for a single-wheel brake. On the rear axle the ratio is 1793.3 N m/bar for a single-wheel brake.

4 EXPERIMENTAL SET-UP

Models of the subsystems within the integrated brake system can be employed to simulate the real system well. However, it is still a better research method to replace the virtual models with real components and to carry out HIL tests.

The simulation of the pneumatic system is difficult because of its complexity. Thus, 'pneumatic-system-in-the-loop' tests are favoured for the research. Figure 7 illustrates the configuration of the test system for the integrated brake system. The

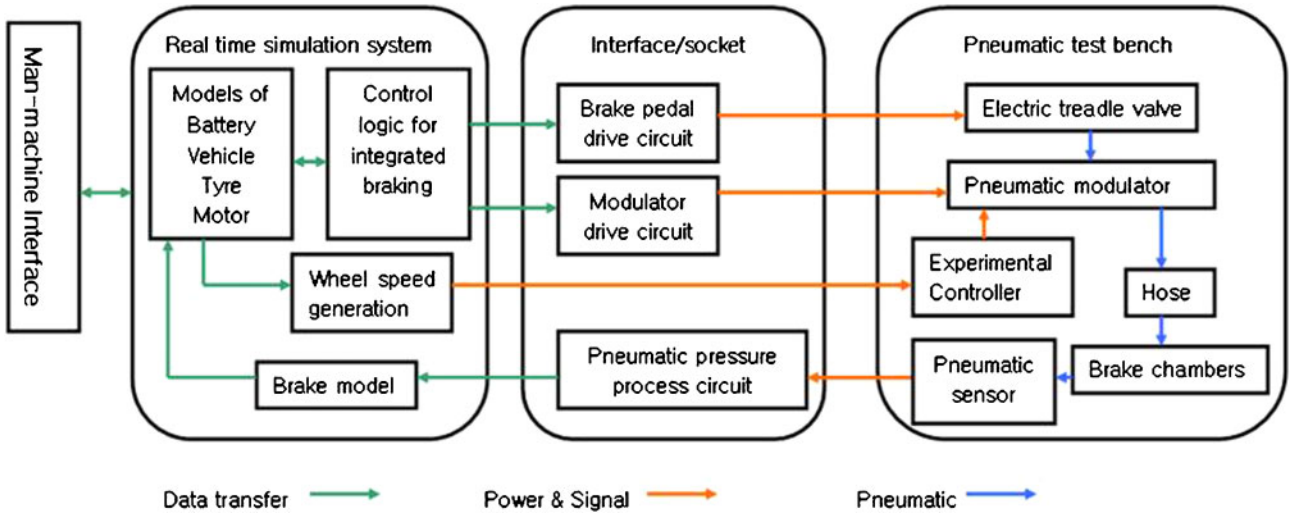

Fig. 7 The configuration of the integrated brake system test system

pneumatic system including the compressor, the air reservoir, the pneumatic modulating valves, and the brake chambers are the same as installed on a city bus in service. The test system consists of the real-time simulation system, the interface socket, and the pneumatic test bench. The real-time simulation system is an Autobox manufactured by DSpace, with a DS1005 processor board and a DS2211 input–output board. The control logic for integrated braking can be included in the Autobox or the experimental controller which is to be installed on the vehicle. Thus, the test system is able to cover several phases of research and development, from the control logic prototyping to the calibration and testing of the control unit. Figure 8 is a photograph of the test system.

5 CONTROL STRATEGY

The integrated control strategy is composed of the strategy on normal braking conditions (no wheel is locked or to be locked) and the strategy during anti-lock braking control. The former including the discussion of different brake-blending methods, has been presented in references [**12**] and [**19**]. It is the integrated control strategy during anti-lock braking that will be discussed here.

5.1 The pneumatic anti-lock braking control strategy for a single wheel

The logic threshold method is believed to be the method applied in most of the ABS, judging by

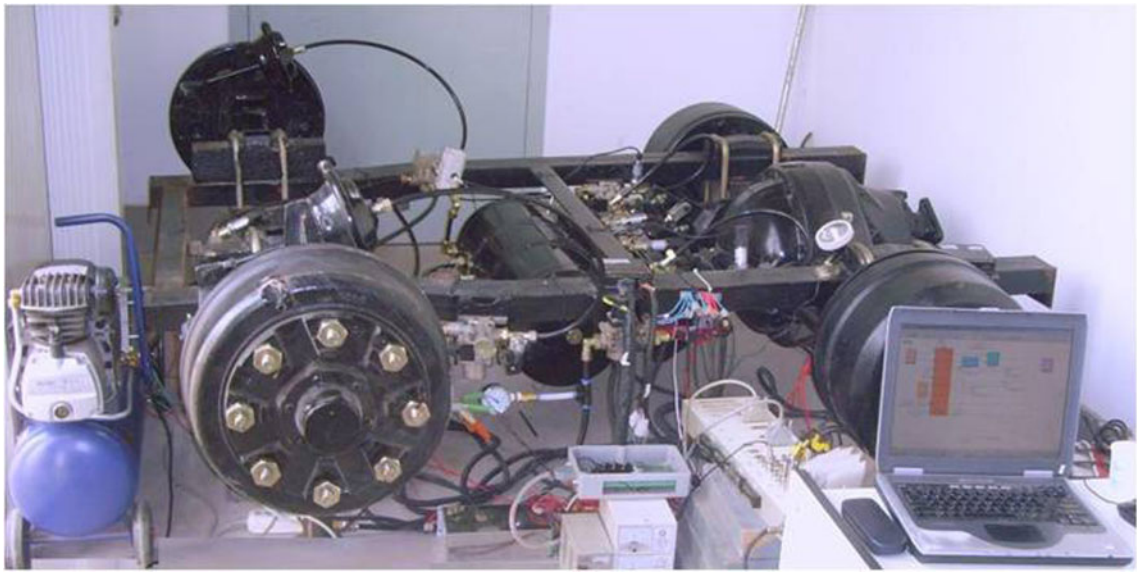

Fig. 8 The test system for integrated brake control

articles and other references. This method monitors the accelerations of the wheels and estimates the vehicle speed. When the accelerations (or decelerations) of the wheels reach the preset thresholds, the ABS carries out particular measures, namely increases, holds, or decreases the brake pressure, in order to keep the wheel slip within a range and to maintain the longitudinal and lateral forces between the wheels and the road surface. The thresholds of the reference slip ratio act as assistant thresholds, amending the orders given out by the acceleration thresholds. The reference slip ratio is calculated from the rotational speed of the wheels and the estimated vehicle speed. Figure 9 illustrates the logic threshold method applied in a WABCO pneumatic ABS.

Based on the revealed control strategies for pneumatic anti-lock braking, a control strategy for a single wheel is proposed here as the basis for integrated control, as shown in Fig. 10.

The control of pneumatic anti-lock braking is divided into eight phases. The eight phases cover the

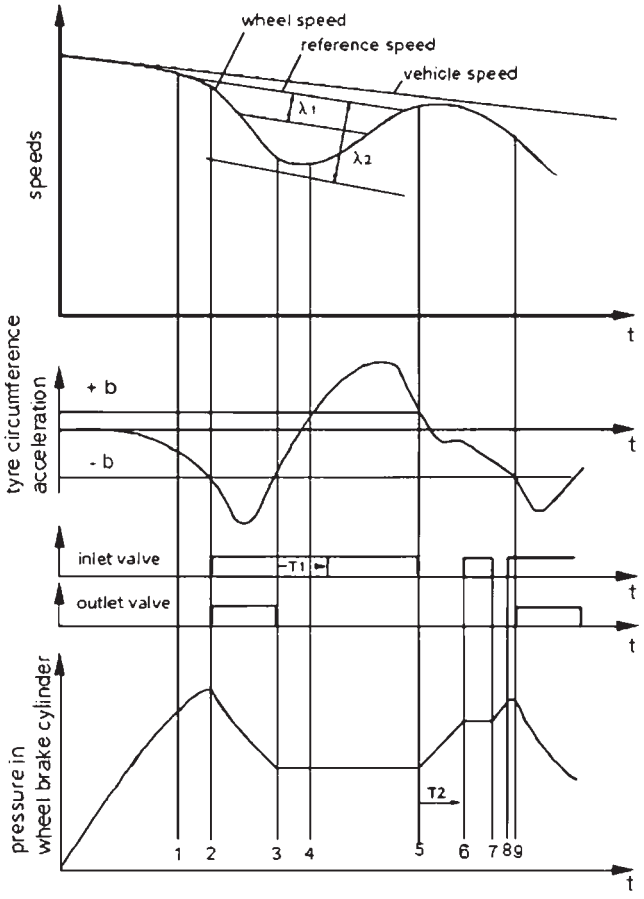

Fig. 9 The logic threshold method applied in a WABCO pneumatic ABS [**18**]

control on low-friction, medium-friction, and high-friction surfaces, indicating that in a single control cycle not every one of the eight phases is gone through. The eight phases can be sorted into 'increase', 'hold', and 'decrease', meaning that in the associated phase the brake pressure is increased, held, or decreased. The thresholds used here include three rotational acceleration thresholds (namely the deceleration threshold a_1 (used as $-a_1$), the lower acceleration threshold a_2, and the higher acceleration threshold a_3) and two reference slip ratio thresholds (namely the lower slip ratio threshold s_1 and the higher slip ratio threshold s_2). All the thresholds mentioned above have positive values.

Phase 1 is a hold phase, which occurs when the deceleration of the wheel becomes lower than $-a_1$. The control logic does not go into phase 2 as a decrease phase until the reference slip ratio reaches s_1, indicating that the wheel is at the edge of being locked, in order to keep the deceleration of the vehicle at a relatively high level. Phase 3 and phase 4 are twin phases which are reached when the deceleration of the wheel decreases so that it is higher than $-a_1$. However, phase 3 is a decrease phase occurring when the slip ratio is higher than s_2, while phase 4 is a hold phase occurring when the slip ratio is lower than s_2. When the friction parameter of the road surface is low, the rotational speed of the wheel is regained more slowly than on a high-friction surface. Phase 3 lowers the slip ratio more actively in this condition, keeping the wheel slip within control. Phase 5 is a hold phase, which can be seen as an extension of phase 4 under good friction conditions when the acceleration of the wheel becomes higher than a_2. On extremely good road surfaces such as dry and clean asphalt, the acceleration of the wheel may reach a high level over a_3, which may reduce the slip ratio too quickly and make the brake force much lower than expected. Then phase 6 occurs to increase the brake pressure. Phase 7 acts as phase 5 when the acceleration that is previously higher than a_3 returns to a value between a_2 and a_3. Phase 8 is an increase phase occurring when the acceleration is lower than a_2, indicating a small difference between the tangential speed of the wheel and the speed of the vehicle. When the wheel begins to decelerate and the deceleration is lower than $-a_1$ again, phase 2 occurs and a new control cycle commences. Note that phase 1 appears only in the very first control cycle.

Thus, on a low-friction surface, a control cycle such as (1–)2–3–4–5–8 is more likely to occur. On a medium-friction surface, a control cycle such as (1–)

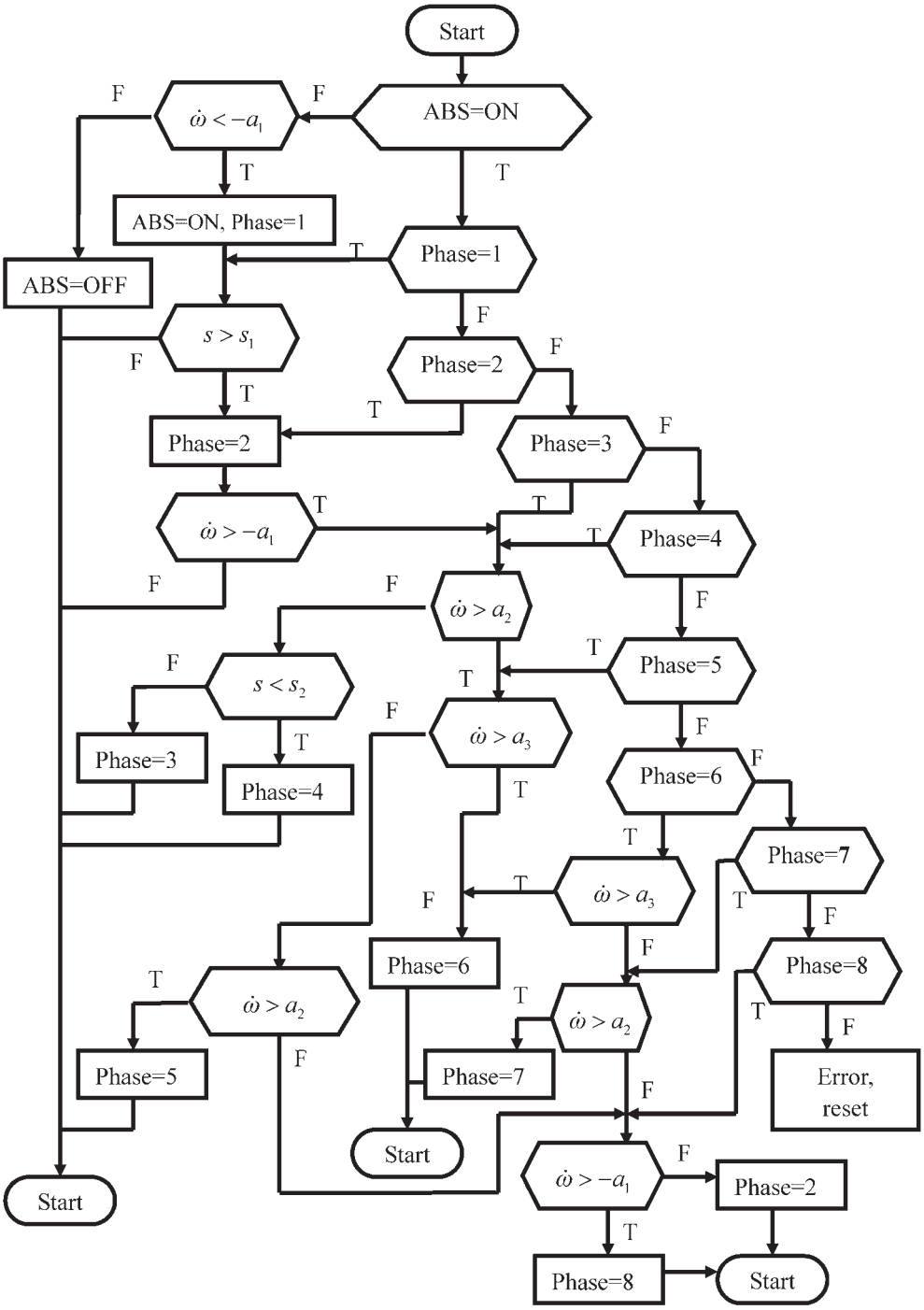

Fig. 10 The control strategy for pneumatic anti-lock braking

2–4–5–8 is more likely to occur. On a high-friction surface, a control cycle such as (1–)2–4–5–6–7–8 is more likely to occur. It is also possible that phase 6 occurs on a low-friction surface and that phase 3 occurs on a high-friction surface owing to the complex relations between the vehicle, the wheels, and the road surface.

5.2 The integrated anti-lock braking control strategy for drive wheels

As mentioned above, the control strategies proposed here are to be applied on hybrid buses and coaches. Thus, the integrated anti-lock braking control strategy is for the two rear drive wheels connected to an electric motor via a final drive.

The control strategy for pneumatic anti-lock braking is the same as in Fig. 10. The braking torque applied by the electric motor is assumed to be shared equally between the two wheels. Thus, the control strategy for regenerative anti-lock braking should take the conditions of both wheels into consideration, as shown in Fig. 11. The rotational acceleration of the left rear wheel is denoted as $\dot{\omega}_F$ and the slip ratio as s_F. Those of the right rear wheel are denoted as $\dot{\omega}_R$ and s_R. The thresholds for both wheels are the same. The significances of the phases in regenerative anti-lock braking control are the

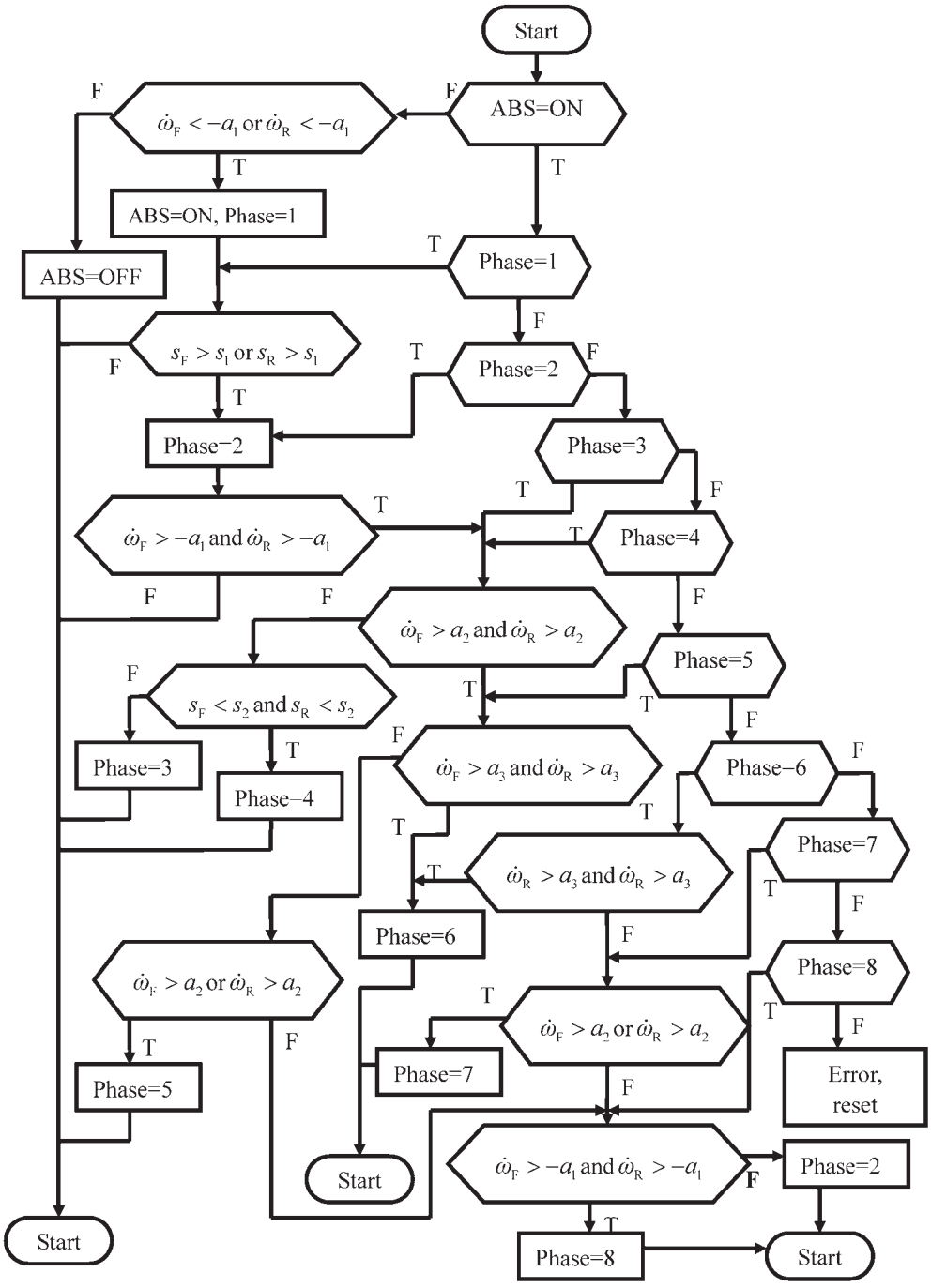

Fig. 11 The control strategy for regenerative anti-lock braking of the rear wheels

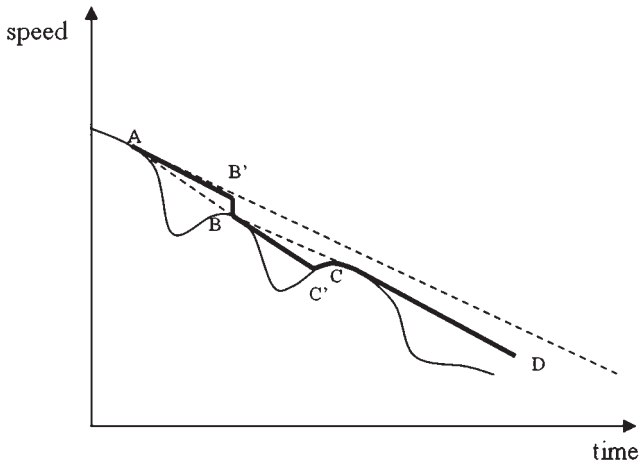

Fig. 12 Estimating the vehicle speed with the speed of wheel and its inflection points

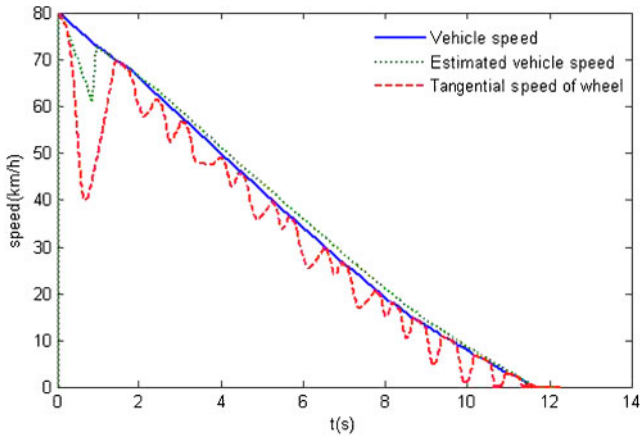

Fig. 13 Estimated the vehicle speed and the estimated slip ratio

same as those in pneumatic anti-lock braking control. The motor torque is limited by its own parameters and the capacity of the battery.

6 SIMULATION AND HIL CONTROL

6.1 Simulation

To evaluate the effect of the integrated control strategy during anti-lock braking, some simulations are carried out in MATLAB–Simulink. The subsystems of the model have been mentioned in section 3.

The scenario for simulation is as follows: with an initial speed of 8 0 km/h, the brake is fully employed, triggering the locking of wheels. As the highest deceleration possible for the HCNG hybrid bus is approximately 0.6 g ($\approx 6\,\mathrm{m/s^2}$), the surfaces used in the simulation are a gravel surface (with a peak equivalent friction parameter of 0.614 and a sliding equivalent friction parameter of 0.557) and a hard-packed snow surface (with a peak equivalent friction parameter of 0.216 and a sliding equivalent friction parameter of 0.136) ensuring that at least the wheels of one axle may be locked.

The pneumatic anti-lock braking strategy is first verified. A simple but effective way of vehicle speed estimation is employed by the control system. In ABS control cycles the speed of the wheel fluctuates frequently. The inflection points of the wheel speed, namely the points when the rotary acceleration of wheel shifts from positive to negative, are very close

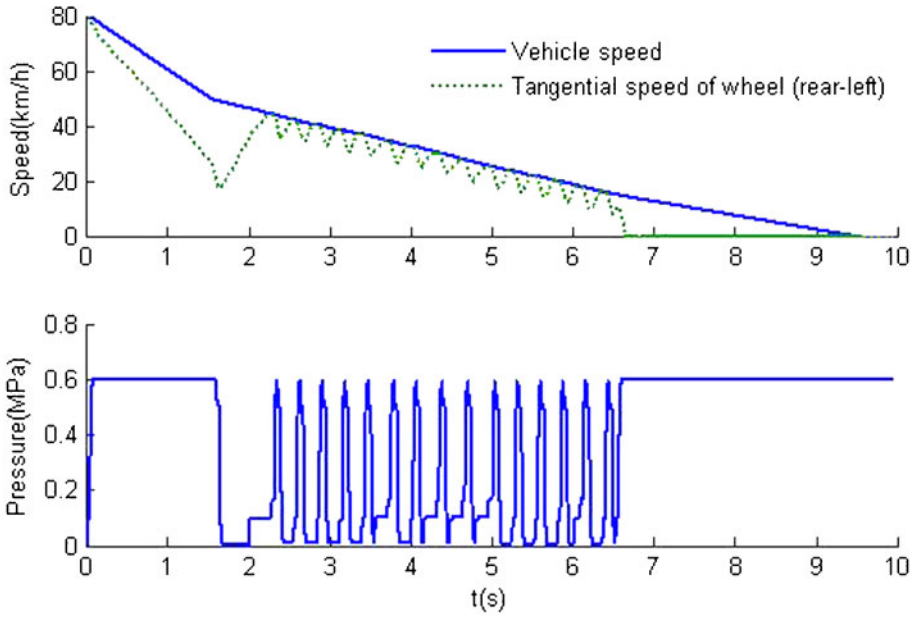

Fig. 14 Results on the jump-μ surface simulation of pneumatic anti-lock braking

to the vehicle speed. Thus, if the last two inflection points are linked with a radial and the latest inflection point is repeately obtained, the vehicle speed can be well estimated. Figure 12 indicates the means of obtaining the estimated vehicle speed, in which the thin solid curve is the speed of the wheel, the dashed lines are the temporary radials from inflection points, and the bold solid curve AB′BC′CD illustrates the estimated vehicle speed.

A difference between the actual speed of vehicle and the estimated speed cannot be totally eliminated. However, the difference is proved to be within the tolerance of the control logic, as shown in Fig. 13. The thresholds for the slip ratio also take the error between the real vehicle speed and the estimated speed into consideration.

The tangential speed of the rear left wheel is also shown in Fig. 13. The speed of the wheel is modulated properly and no lock occurred. It is notable that, at the start of braking, the speed of the wheel drops abruptly. This is due to the inaccuracy in the estimated vehicle speed for the time being and

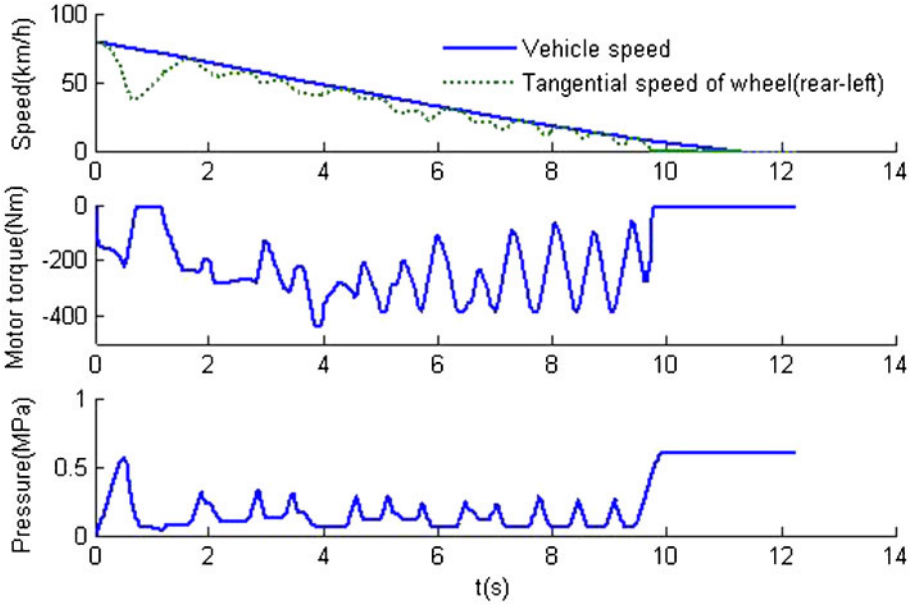

Fig. 15 Results on the low-friction surface simulation of integrated anti-lock braking

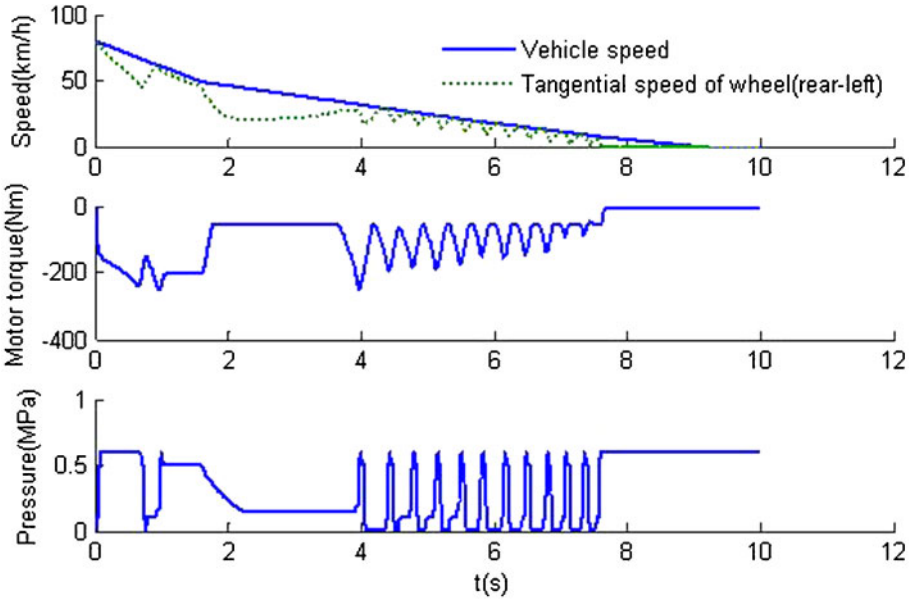

Fig. 16 Results on the jump-μ surface simulation of integrated anti-lock braking

the entrance logic of anti-locking braking (namely phase 1 of the strategy). The other three wheels are not locked as well.

Figure 14 illustrates the simulation of the pneumatic anti-lock braking strategy on a jump-μ surface. On the medium-friction surface the wheel begins to

Table 2 Comparison of pneumatic anti-lock braking and integrated anti-lock braking

	Average deceleration (m/s^2)	Average jerk (m/s^3)	Average pneumatic pressure (bar)	Energy regenerated (kJ)	80 km/h to 0 km/h displacement (m)
Pneumatic anti-lock braking	−1.95	3.36	2.00	—	120.2
Integrated anti-lock braking	−2.04	2.88	1.39	14.1	117.4

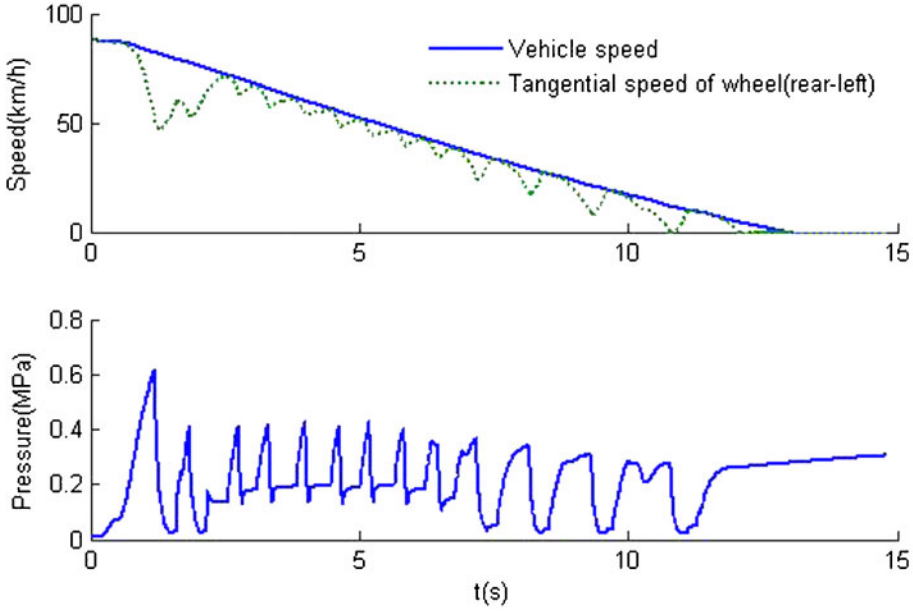

Fig. 17 Results of low-friction surface HIL tests under pneumatic anti-lock braking

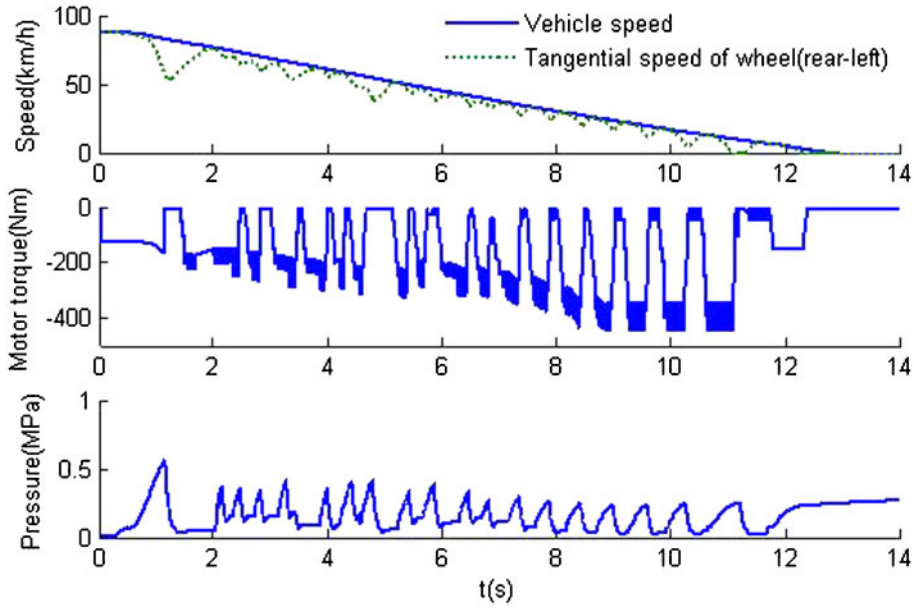

Fig. 18 Results of low-friction surface HIL tests under integrated anti-lock braking

show signs of locking and then regains its speed because of modulation of anti-lock braking. The wheel moves on to the low-friction surface and is near to unstable for a while. Shortly after that, the wheel is under the control of anti-lock braking periodically and is not locked. The brakes of the other three wheels are also modulated properly to avoid any wheel locking.

The pneumatic anti-lock braking strategy has proved to be effective. The integrated anti-lock braking strategy is simulated following the same procedure to make a comparison. The initial SOC of the battery is set equal to 0.3. Figure 15 illustrates the result of simulation. It is notable that the fluctuation in the wheel speed is smoothed by modulating the motor torque. The pneumatic pres-

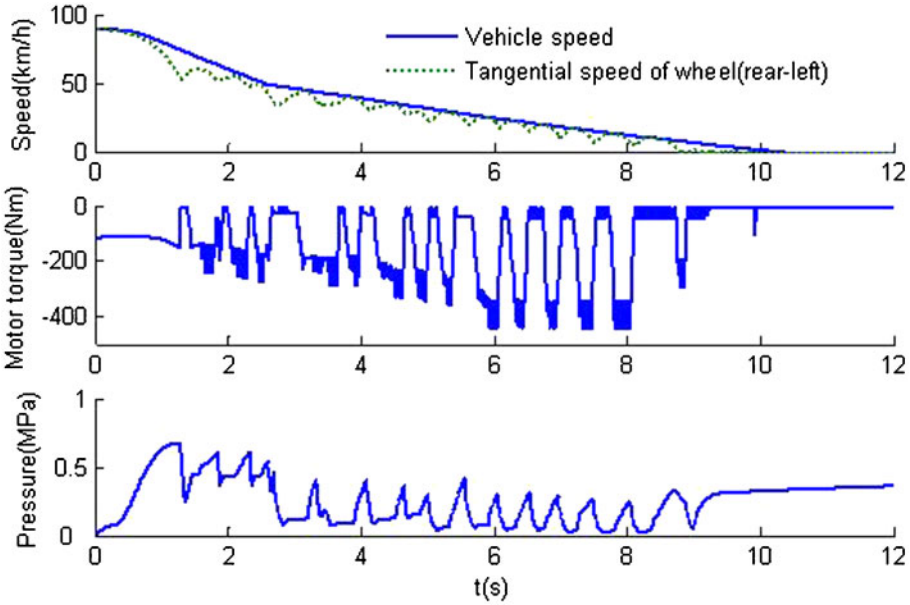

Fig. 19 Results of jump-μ surface HIL tests under integrated anti-lock braking (rear left wheel)

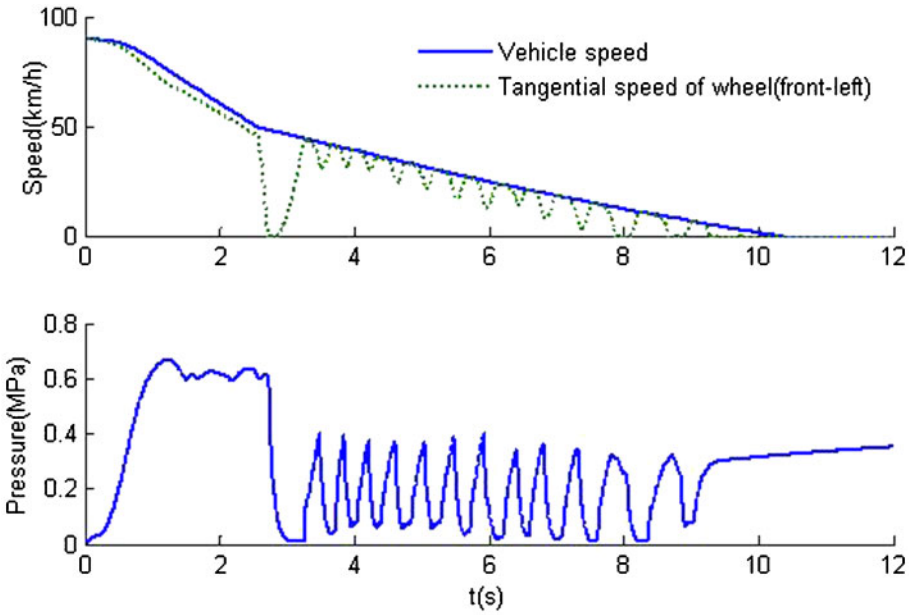

Fig. 20 Results of jump-μ surface HIL tests under integrated anti-lock braking (front left wheel)

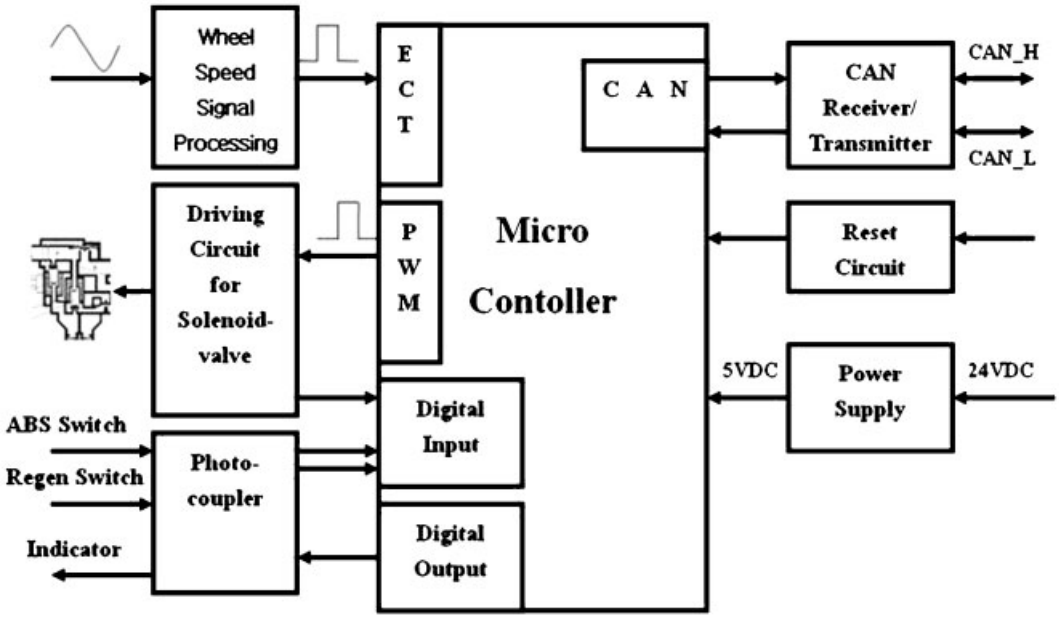

Fig. 21 Functional diagram of the integrated brake controller (ECT, electronic control unit; PWM, pulse width modulator)

sure is also decreased evidently. The results of the jump-μ surface simulation are shown in Fig. 16. The wheel speed is modulated properly as well. In no case is a single wheel locked.

The results from the low-friction surface simulation of pneumatic anti-lock braking and those of integrated anti-lock braking are compared specifically in Table 2. Although the stopping distances and the average decelerations for both kinds of anti-lock braking are almost the same, integrated anti-lock braking reduces the fluctuation in the vehicle acceleration effectively. The pneumatic pressure needed by the pneumatic brake during anti-lock braking is also much lower. Thus, integrated anti-lock braking ensures not only a better ride for passengers but also a quicker response of the pneumatic brake, owing to the quicker inflation of the brake chamber diaphragm when the required brake pressure is lower.

6.2 HIL tests

The pneumatic anti-lock braking strategy is tested first on the test bench. The result is shown in Fig. 17. The fluctuation in the pneumatic pressure is much greater than in the simulation. The wheel speed also drops more than in the simulation. The overall effect of anti-lock braking control is satisfactory. No wheel is locked during deceleration.

The test results of integrated anti-lock braking control are illustrated in Fig. 18. The pattern of wheel speed fluctuation resembles that under pneumatic anti-lock braking. The modulation of the pneumatic pressure is relatively moderate.

Jump-μ surface HIL tests are also carried out under integrated anti-lock braking. The results are illustrated in Figs 19 and 20. No rear wheel is locked in the tests. Although the front wheels are locked at the moment of the μ jump, as shown in Fig. 19, the speeds of the wheels are regained very quickly. Thus,

Fig. 22 The experimental integrated brake controller

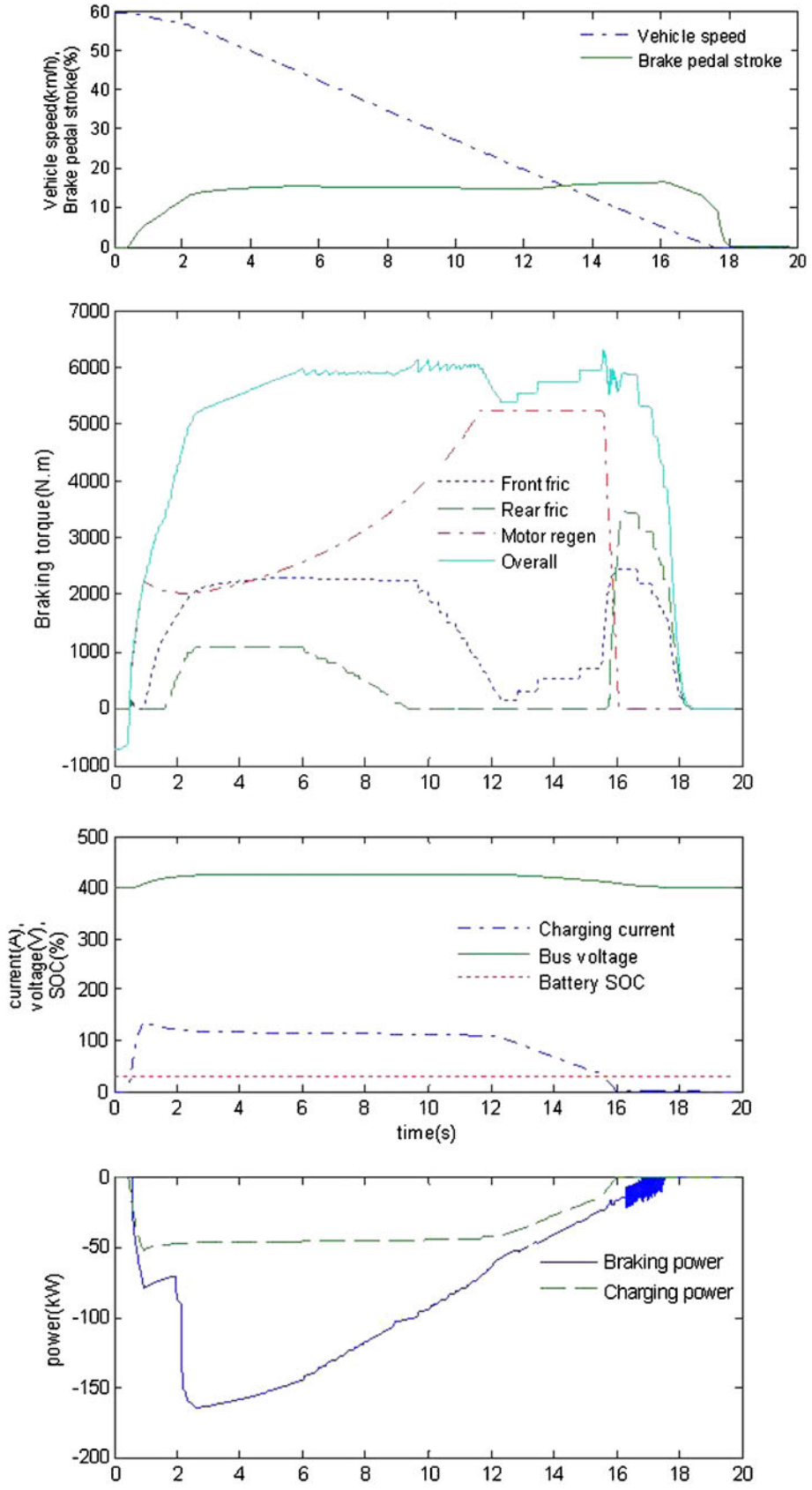

Fig. 23 Results of a series of brake-blending HIL tests

the stability of the vehicle is still maintained during deceleration.

In comparison with pneumatic anti-lock braking based on HIL test results, integrated anti-lock braking is still advantageous in the vehicle ride and the agility of the pneumatic pressure. For example, the average jerk is 3.349 m/s^3 under pneumatic control and 3.123 m/s^3 under integrated control. The average pneumatic pressure under pneumatic control is 1.9 bar and under integrated control is 1.6 bar.

7 BRAKE CONTROL WITH AN INTEGRATED BRAKE CONTROLLER

7.1 The development of the experimental brake controller

To carry out integrated brake control on board, an integrated brake controller is needed. In order to facilitate transfer on to hybrid city buses in the near future, the controller is designed so as to be compatible with the pneumatic ABS controller originally installed, with respect to the form of sockets, the driving of the solenoid-modulating valves, and the processing of the wheel speed sensor signals.

The controller consists of the digital core and some processing–driving circuits. The digital core is usually a microcontroller with its peripheral circuits. The most important processing circuit is the wheel speed signal-processing circuit, while the most important driving circuit is the solenoid-modulating valve-driving circuit. In addition the inputs and outputs for braking energy regeneration are carried out by a controller area network (CAN), namely the stroke of the brake pedal, the limit of the electric motor torque, and the required regenerative motor torque, mainly with the vehicle control unit and the motor control unit.

The functional diagram of the proposed controller is illustrated in Fig. 21. The microcontroller is chosen as the Freescale MC9S12XDP512. It has the function modules required by the integrated brake controller such as an enhanced capture timer, a pulse-width modulation output, and CAN communication.

The output of the wheel speed sensors are waves resembling sine waves with noises. The waves are usually processed and transformed into square waves with clear frequency signals and then captured by the capture timer module of the microcontroller. In order to screen the noises thoroughly, a processing circuit with two phases of low-pass filter and two phases of comparator with backlash is proposed.

The driving circuit for the solenoid-modulating valves is simply a power-amplifying circuit with a diagnosing function. A twin-channel high-side switch with open-drain diagnostic port for each channel from Infineon is chosen.

Figure 22 is a photograph of the experimental integrated brake controller.

7.2 HIL tests with the integrated brake controller

In the previous HIL tests the control strategy is carried out by the DSpace real-time simulator. A control unit is definitely smaller than a DSpace but is usually not so reliable. In order to simulate the integrated braking control on board, a set of HIL tests is carried out using the experimental controller.

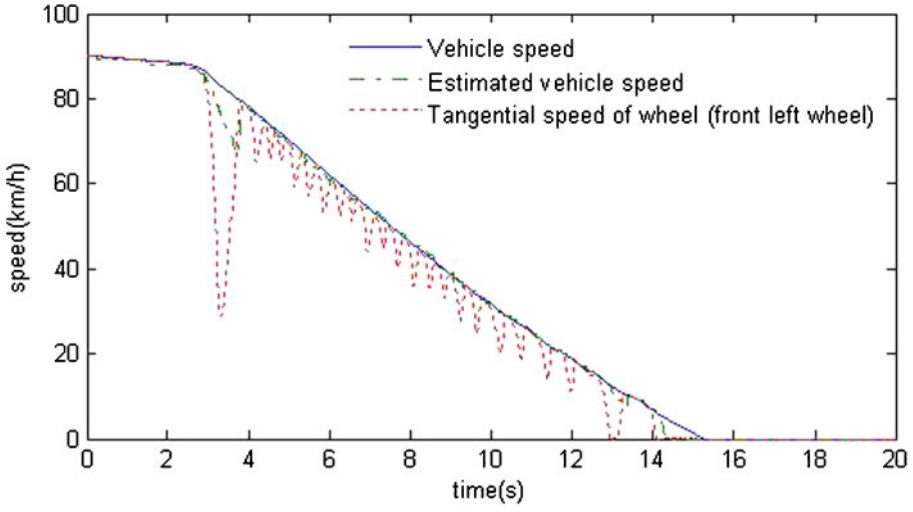

Fig. 24 Results of vehicle speed estimation

During normal decelerations, the controller controls the modulating valves directly and requires a regenerative braking torque of the electric motor, thus carrying out the series brake-blending strategy. Figure 23 illustrates the results of a series of brake-blending HIL tests. In the deceleration the brake pedal is controlled by the driver. The overall braking torque, composed of the frictional braking torques of the four wheels and the regenerative braking torque of the electric motor (converted to the braking torques exerted on the wheels), is proportional to the stroke of the brake pedal. The charging power

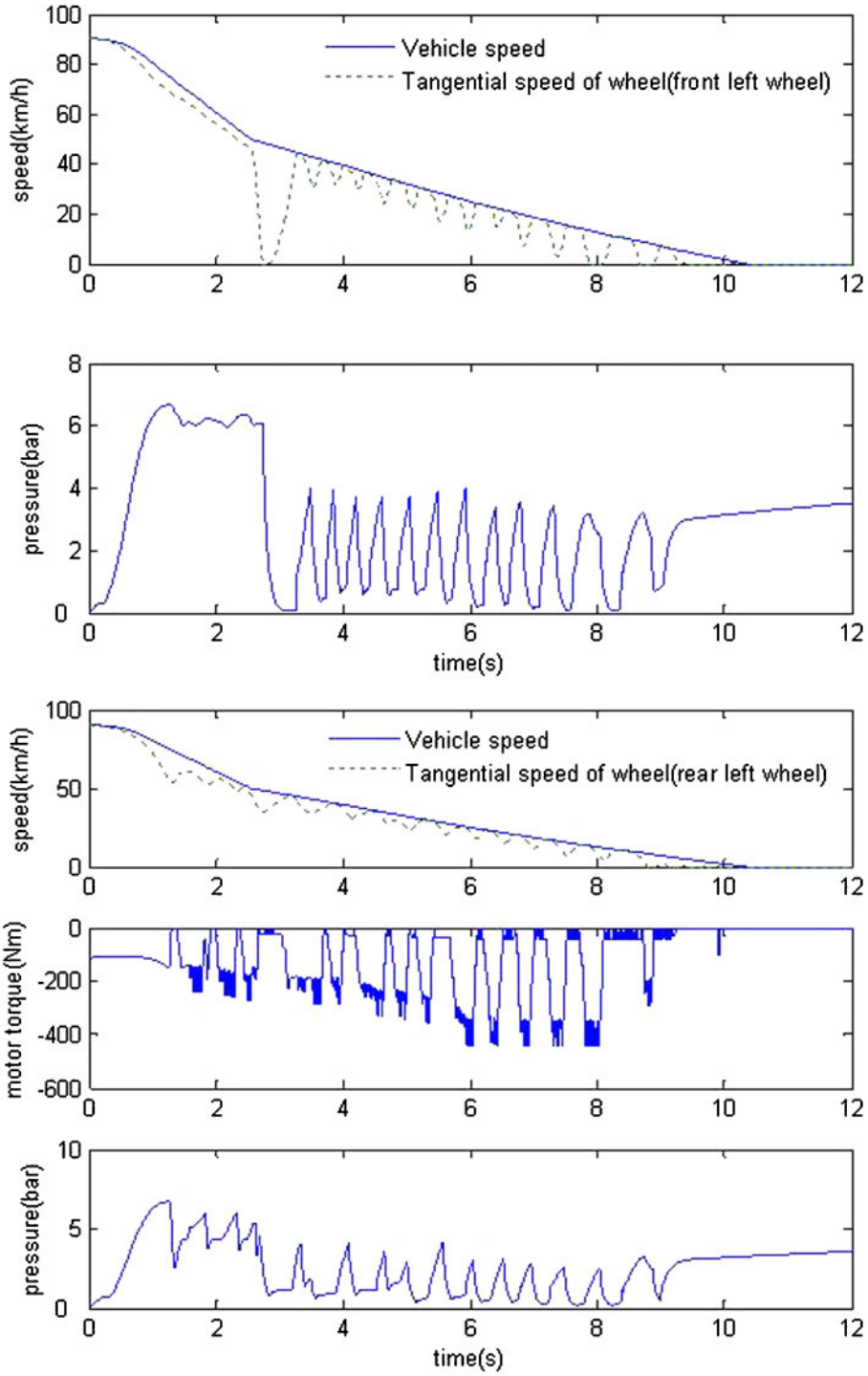

Fig. 25 Results of jump-μ surface HIL tests with an integrated brake controller under integrated anti-lock braking

Table 3 Comparison of pneumatic anti-lock braking and integrated anti-lock braking with the experimental brake controller

	Average deceleration (m/s^2)	Average jerk (m/s^3)	Average pneumatic pressure (bar)	Energy regenerated (kJ)	80 km/h to 0 km/h displacement (m)
Pneumatic anti-lock braking	−1.66	3.15	2.05	—	119.1
Integrated anti-lock braking	−1.77	3.12	1.57	54.8	118.1

into the battery is related to the torque and the speed of the motor, which is connected via a transmission and a final drive to the two rear wheels in a series hybrid city bus. A braking energy of 1204 kJ is to be dissipated by brakes, of which 44 per cent or 530 kJ is regenerated by the electric motor and charges the battery.

When there is a danger of wheel locking, the integrated brake controller modulates the modulating valves and the regenerative braking torque under the anti-lock braking mode. In anti-lock braking control, the estimated vehicle speed is very important for the calculation of the estimated slip ratio of each of the wheels. Figure 24 illustrates the results of vehicle speed estimation by the controller with the estimation logic coded and downloaded.

Either using pneumatic anti-lock braking control logic or integrated anti-lock braking logic, the integrated brake controller controls the brake system effectively and ensures the braking safety of the vehicle. The HIL test results on integrated anti-lock braking control on a jump-μ surface are illustrated in Fig. 25. In comparing the results on anti-lock braking control with those of pneumatic logic and integrated logic, the advantage of integrated anti-lock braking control is still obvious using the experimental controller. The HIL test results on a low-μ surface are listed in Table 3.

8 CONCLUSION

Based on a series regenerative braking system, an integrated brake system combining regenerative braking of the electric motor and friction braking of the pneumatic brakes is proposed. The system employs the same set of valves to modulate the pneumatic pressure during brake blending and anti-lock braking control. A control strategy is proposed for anti-lock braking control of the friction braking and regenerative braking. Simulations are carried out on authorized models. HIL tests are carried out on a test bench featuring the pneumatic brake system of a city bus. An integrated brake controller is also designed for carrying out the series brake blending and integrated anti-lock braking control on board and is tested on the test bench.

The results of simulation and HIL tests show that integrated anti-lock braking control is advantageous in ride comfort and quick response of the pneumatic system. It also ensures stability and safety of the vehicle. At present, a fraction of braking energy can be regenerated.

A further study could be carried out on the influence of anti-lock regenerative braking on the powertrain, the optimization of the integrated control strategy, and the influence of integrated anti-lock braking on the lateral stability of a vehicle.

REFERENCES

1 **Gao, Y.** and **Ehsani, M.** Investigation of the effectiveness of regenerative braking for EV and HEV. SAE paper 1999-01-2910, 1999.
2 **Ehsani, M., Gao, Y.,** and **Butler, K. L.** Application of electrically peaking hybrid (ELPH) propulsion system to a full size passenger car with simulated design verification. *IEEE Trans. Veh. Technol.*, 1999, **48**(6), 1779–1787.
3 Hybrid check list: what kind of hybrid is it? Available from http://www.hybridcenter.org/hybrid-center-how-hybrid-cars-work-under-the-hood.html.
4 **Panagiotidis, M., Delagrammatikas, G.,** and **Assanis, D.** Development and use of a regenerative braking model for a parallel hybrid electric vehicle. SAE paper 2000-01-0995, 2000.
5 **Pickenhahn, J., Gilles, L., Hönig, T.,** and **Thomas, P.** Concepts for regenerative braking in vehicles with hybrid propulsion drive. In Proceedings of the 26th International μ Symposium, 20 August 2007, pp. 253–288.
6 In the AutoblogGreen garage: 2008 Honda Civic hybrid, 2008, available from http://www.autobloggreen.com/2008/08/11/in-the-autobloggreen-garage-2008-honda-civic-hybrid/.
7 NHSA Standard 121. *Air brake systems – trucks, buses, and trailers*, 1 January 1975 (US Department of Transportation, National Highway Traffic Safety Administration, Washington, DC).
8 **Bartlett, W. D.** Calculation of deceleration rates for S-cam air-braked heavy trucks equipped with anti-lock brake systems. SAE paper 2007-01-0714, 2007.
9 **Kusano, A.** *Brake pressure control device for automotive vehicles*. US Pat. 6,290,310, 2000.

10 **Fey, W., Fachinger, G., Engelmann, M., Klein, A.,** and **Schubert, P.** *Electrohydraulic brake system*. US Pat. 6,817,681, 2001.

11 **Tagata, K., Sakai, K., Aoki, Y., Suzuki, K.,** and **Nakano, H.** *Vehicle brake device*. US Pat. 7,360,360, 2007.

12 **Chu, L., Zhang, Y. S., Zhu, Y. J., Lv, X. Y., Guo, Y. J.,** and **Ming, S. M.** *Pneumatic anti-lock braking system for hybrid commercial vehicles*. Chin. Pat. Applic. 200610017245.0, 2007.

13 **Zhang, J., Lu, X., Zhang, P.,** and **Chen, X.** Road test of hybrid electric bus with regenerative braking system. *Jixie Gongcheng Xuebao* (*J. Mech. Engng*), 2009, **45**(2), 25–30.

14 **Gim, G.** and **Nikravesh, P. E.** An analytical model of pneumatic tyres for vehicle dynamic simulations. Part 1: pure slips. *Int. J. Veh. Des.*, 1990, **11**(6), 589–618.

15 **Gim, G.** and **Nikravesh, P. E.** An analytical model of pneumatic tyres for vehicle dynamic simulations. Part 3: validation against experimental data. *Int. J. Veh. Des.*, 1991, **12**(2), 217–228.

16 **Bohm, F.** Mechanik des Gurtelreifens. *Ingenicar Arch.*, 1966, **35**, 82–101.

17 **Subramanian, S. C., Darbha, S.,** and **Rajagopal, K. R.** Modeling the pneumatic subsystem of an S-cam air brake system. *Trans. ASME, J. Dynamic Systems, Measmt Control*, 2004, **126**(1), 36–46.

18 *ABS/ASR „D"-„Cab" – version anti-lock braking system for commercial vehicles,* 1st edition, 2006 (WABCO, Brussels).

19 **Zhang, J., Lu, X., Chen, S.,** and **Zhang, P.** Coordinated control for regenerative braking system. In Proceedings of the Vehicle Power and Propulsion Conference (*VPPC '08*), 3–5 September 2008, pp. 1–6 (IEEE, New York).